Numerical Analysis of High-Brightness Tapered Ridge-Waveguide Lasers

J.-P. Koester*†, H. Wenzel*, M. Wilkens*, and A. Knigge*
*Ferdinand-Braun-Institut (FBH), Gustav-Kirchhoff-Str. 4, 12489 Berlin, Germany
†Email: jan-philipp.koester@fbh-berlin.de

***Abstract*—In this work, we present a simulation-based analysis of a CW driven tapered ridge-waveguide laser having a high lateral brightness of $5\,\mathrm{W}\cdot\mathrm{mm}^{-1}\mathrm{mrad}^{-1}$ at $2.5\,\mathrm{W}$ optical output power.**

***Index Terms*—High-brightness diode laser, Lateral mode filter, Tapered ridge-waveguide laser**

I. Introduction

The output power of CW-driven ridge-waveguide lasers is mainly limited by its facet load and thermal power saturation. Both effects can be reduced by increasing the biased lateral dimension. This, however, increases the number of supported lateral modes and eventually decreases the beam quality [1]. Therefore, the round-trip gain of unwanted higher-order lateral modes has to be limited.

One possibility is to change the lateral electrical contact and waveguide width in the longitudinal direction. Thereby, the minimal ridge width and, therefore, the number of supported local lateral modes can be reduced by simultaneously achieving an overall larger electrical contact area. Recently, a lateral brightness of $5\,\mathrm{W}\cdot\mathrm{mm}^{-1}\mathrm{mrad}^{-1}$ at $2.5\,\mathrm{W}$ output power using a tapered ridge-waveguide (TRW) laser design was reported [2].

In this work, we investigate a TRW laser diode, as used in Ref. [2] and depicted in Fig. 1, emitting at $970\,\mathrm{nm}$ using the traveling-wave based simulation tool WIAS-BALaser which takes into account all relevant carrier and temperature effects [3]. Subsequently, the resulting time-averaged complex index profile is used to perform an intra-cavity modal analysis as well as a beam-propagation method (BPM) based cavity round-trip investigation to reveal the design-related lateral mode filter properties.

II. Longitudinal-lateral device design

The investigated laser design is shown in Fig. 1. Here, the ridge width w increases from $w_\mathrm{r} = 5\,\mu\mathrm{m}$ at the rear to $w_\mathrm{f} = 23\,\mu\mathrm{m}$ at the front facet. This is achieved by a $L_\mathrm{t} = 4.4\,\mathrm{mm}$ long linear taper connecting a straight rear and front waveguide having a length of $1\,\mathrm{mm}$ and $0.6\,\mathrm{mm}$, respectively. The width B of the index guiding trenches changes linearly within the tapered section such that $M = w + B = 27\,\mu\mathrm{m}$ is held constant over the whole device length. Applying the effective index method, the index trenches result in Δn_eff of 0.004. The rear and front facet were modeled to have power reflectivity values of $98\,\%$ (HR) and $0.1\,\%$ (LR), respectively. For more information on the device we refer to Ref. [2].

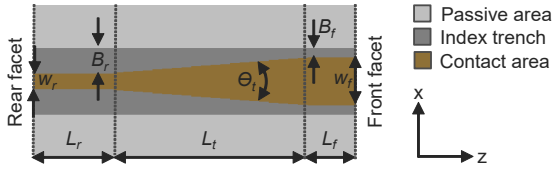

Fig. 1. Schematic lateral-longitudinal (x-z) representation of the tapered ridge-waveguide laser under investigation including all relevant design parameters.

III. Simulation procedure

The laser simulations were performed using WIAS-BALaser [3]. Here, the forward and backward traveling slowly varying fields $u^{\pm}(x,z,t)$ within the lateral-longitudinal (x-z) plane (see Fig. 1) are described by paraxial traveling wave equations assuming a reference index n_b and frequency ω_0. The optical model is coupled to equations governing the transport of the charged carriers. The lateral drift-diffusion of excess carriers within the active region is modeled by an effective diffusion factor, and current spreading inside the p-doped region is modeled via the Laplace equation. The temperature distribution is calculated by iteratively solving the stationary heat flow equation for the self-consistently obtained time-averaged heat sources within each vertical-lateral cross-section of the laser.

The simulated time-averaged photon density $||u(x,z)||^2$, carrier density $N(x,z)$ and temperature $T(x,z)$ as well as the built-in refractive index profile $n_0(x,z)$ defined by the index-guiding trenches were used to calculate a resulting complex index profile $n(x,z)$ as described in Ref. [4]. Subsequently, the local 1D lateral TE modes Φ_m of the resulting waveguide were calculated solving the underlying eigenvalue problem giving information about the number of local guided and radiation modes, including its modal index and gain. Finally, the cross-coupling between different waveguide modes after propagating one round-trip was investigated using a scalar 2D finite-difference BPM.

IV. Results

Fig. 2 shows the simulated (solid lines) and measured (partially transparent lines) output power P and beam quality factor $M^2_{95\%}$ as a function of the applied current I. The simulations reveal that the increase of $M^2_{95\%}$ around $I = 1\,\mathrm{A}$ ($P \approx 1\,\mathrm{W}$) is caused by the onset of the first higher-order lateral mode. By further increasing the current injection level, $M^2_{95\%}$ only slightly increases. The following results focus on the working point at $I = 3\,\mathrm{A}$ leading to $P \approx 2.5\,\mathrm{W}$.

978-1-6654-7899-1/22/$31.00 ©2022 IEEE

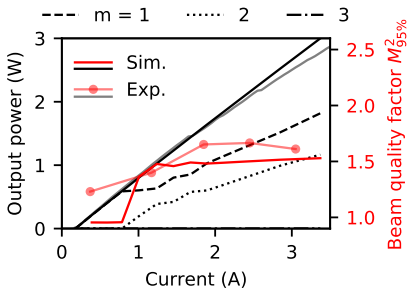

Fig. 2. Simulated (WIAS-BALaser) and measured output power and beam quality factor as function of the injection current.

Fig. 3 (a) and (b) show the index and gain profiles (solid lines) at the rear and front facet as calculated from BALaser results. The elevated refractive index values and the lower gain at the front compared to the rear are caused by the nonuniform longitudinal temperature, and carrier density distributions [4]. In addition, the modal index and gain obtained by solving the 1D Helmholtz equation for these profiles are shown as structured horizontal lines. It follows that the waveguide at the rear facet only supports two guided modes. Furthermore, the fundamental mode experiences a higher modal gain than the first higher-order mode caused by its larger spatial overlap with the absorptive regions next to the contact stripe. This is in contrast to the modes at the front facet. Here, the lateral carrier accumulation leads to an increased modal gain for higher-order modes compared to the fundamental mode. In panel (c), the relative modal gain $\frac{g_m - g_1}{g_1}$ is plotted as function of z revealing that higher-order modes show an increasing gain toward the front. However, only the two first modes are guided in the rear waveguide leading to high round-trip losses for modes with $m \geq 3$.

The modal round-trip losses, as well as the modal cross-coupling, were further analyzed using a BPM. Here, we exemplary show the back and forward propagation of the second higher-order lateral mode $\Phi_3(x, L)$ obtained at the front facet $z = L$ as input. In the top panel of Fig. 4, the resulting

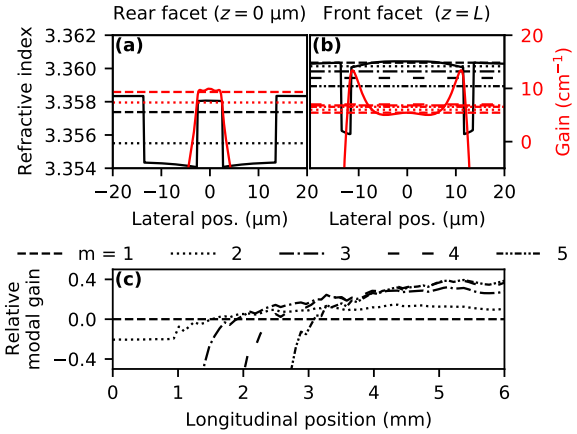

Fig. 3. Index and gain profiles at the rear (a) and front (b) facet at $P \approx 2.5\,\mathrm{W}$. The resulting modal index and gain is depicted as horizontal lines. Panel (c) presents the longitudinal resolved relative modal gain of the first five local lateral waveguide modes.

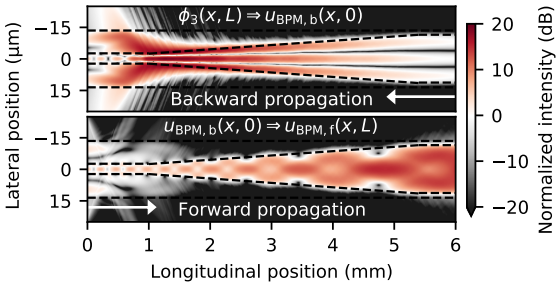

Fig. 4. Intensity distributions $|u|^2$ obtained by BPM calculations. Top: Backward propagation $u_{\mathrm{BPM,b}}$ of $\Phi_3(x, L)$. Bottom: Forward propagation $u_{\mathrm{BPM,f}}$ of the field profile $u_{\mathrm{BPM,b}}(x, 0)$.

intensity profile $|u_{\mathrm{BPM,b}}|^2$ is shown. In agreement with the rapidly decreasing relative modal gain in Fig. 3 (c), most of the modal power is radiated at $z < 1.5$ mm. The spatial overlap of the resulting field $u_{\mathrm{BPM,b}}(x, 0)$ at the rear facet with the corresponding local lateral modes $\Phi_m(x, 0)$ indicates that $13\,\%$ of the power gets coupled into the fundamental mode. The remaining power, however, is contained in several radiation modes. The intensity profile of the forward propagation of $u_{\mathrm{BPM,b}}(x, 0)$ is shown in the bottom part of Fig. 4. After a full round-trip the field at front facet $u_{\mathrm{BPM,f}}(x, L)$ predominantly $(80\,\%)$ consists of the fundamental mode. However, $20\,\%$ of the power is still carried by the second higher-order mode. Nevertheless, $\Phi_3(x, L)$ experiences no amplification but rather gets attenuated by about $-1.5\,\mathrm{dB}$ after one round-trip which prevents it from reaching the laser threshold.

V. Conclusion

We presented a simulation-based analysis of a CW-driven TRW laser. The complex refractive index distribution obtained using a sophisticated laser model was further investigated by performing a modal and BPM analysis. Following this approach, we showed that higher-order lateral modes experience an increasing relative modal gain towards the front but get partially radiated during their propagation through the resonator. The resulting high round-trip losses prevent those unwanted modes reaching laser threshold.

Acknowledgment

The authors want to thank G. Erbert for the discussions contributing to this work.

References

[1] J.-P. Koester, A. Putz, H. Wenzel, H.-J. Wünsche, M. Radziunas, H. Stephan, M. Wilkens, A. Zeghuzi, and A. Knigge. Mode competition in broad-ridge-waveguide lasers. *Semicond. Sci. Technol.*, 36(1):015014, November 2020.

[2] M. Wilkens, G. Erbert, H. Wenzel, A. Maaßdorf, J. Fricke, P. Ressel, A. Knigge, and P. Crump. Highly Efficient High-Brightness 970-nm Ridge Waveguide Lasers. *IEEE Photon. Technol. Lett.*, 32(7):406–409, April 2020.

[3] Mindaugas Radziunas. Modeling and simulations of broad-area edge-emitting semiconductor devices. *Int J High Perform Comput Appl*, 32(4):512–522, July 2018.

[4] J.-P. Koester, M. Radziunas, A. Zeghuzi, H. Wenzel, and A. Knigge. Traveling wave model-based analysis of tapered broad-area lasers. In *Physics and Simulation of Optoelectronic Devices XXVIII*, volume 11274, page 112740I. International Society for Optics and Photonics, March 2020.